Corrosion Science 226 (2024) 111668

Contents lists available at ScienceDirect

Corrosion Science

journal homepage: www.elsevier.com/locate/corsci

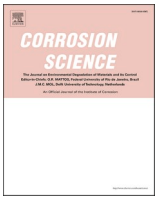

Inter-melt pool corrosion and repassivation of SS316L stainless steel processed by laser powder bed fusion

Karthikeyan Hariharan *, Xiaolei Guo, Hsien-Lien Huang, Narasi Sridhar, Jayendran Srinivasan, Jinwoo Hwang, Gerald S. Frankel, Eric J. Schindelholz *

Department of Materials Science and Engineering, The Ohio State University, Columbus, OH, USA

ARTICLE INFO

Keywords:
Segregation (C)
Pitting corrosion (C)
Interfaces (C)
Passivity (C)
STEM (B)

ABSTRACT

Pit stability and repassivation of SS316L stainless steel processed by laser powder bed fusion (L-PBF) were examined through polarization experiments on one-dimensional (1D) pit electrodes. The L-PBF-SS316L pit was observed to grow along the Cr and Mo-depleted melt pool boundaries (MPBs) well below the nominal repassivation potential (E_{rp}) due to partial repassivation. MPBs promote pit stability in L-PBF-SS316L by offering an easy path for pit propagation. The implications on the reliability of the nominal E_{rp} of L-PBF-SS316L as a metric for localized corrosion resistance are discussed.

1. Introduction

The resistance of SS316L stainless steel (SS316L) manufactured by additively manufacturing processes such as laser powder bed fusion (L-PBF) to environmental degradation can differ considerably from conventionally processed counterparts. There have been numerous studies on pitting corrosion of L-PBF-SS316L stainless in various environments in the last decade. High pitting potentials (E_{pit}) of L-PBF-SS316L have been reported (> 0.6 V_{SCE}), suggesting enhanced pitting resistance, which is often attributed to suppression of deleterious MnS inclusions due to rapid solidification in the L-PBF process [1–7]. Moreover, the oxide inclusions in the L-PBF stainless steels are refined to the submicron- or nano-scale, which inhibits pit initiation at matrix/-inclusion interfaces [2,8].

A feature that has garnered little attention is the fact that the repassivation potential (E_{rp}) of L-PBF-SS316L is equal to or lower than that of wrought SS316L [1,2,7]. Consequently, the ($E_{pit} - E_{rp}$) window for stable pit growth is significantly larger for L-PBF-SS316L than for wrought SS316L. Sander et al. found that ($E_{pit} - E_{rp}$) was ~ 0.8 V for L-PBF-SS316L but only 0.3 V in wrought SS316L [2]. Chao et al., who reported extraordinarily high pitting potentials of L-PBF-SS316L (> 0.6 V_{SCE}), were unable to measure E_{rp} in their cyclic potentiodynamic polarization (CPP) experiments because the reverse scan current remained high even below the forward scan open circuit potential (OCP) (~ 0 V_{SCE}) [1]. On the other hand, wrought SS316L repassivates at −50 mV_{SCE}, well-above its forward scan OCP. Similarly, Laleh et al. also reported that the E_{rp} of L-PBF-SS316L was lower than its forward scan OCP despite possessing a high E_{pit} of 0.7 V_{SCE} [7]. The authors also found that the E_{rp} of the wrought SS316L was higher than its L-PBF counterpart and about 100 mV above its own OCP.

The above discussion suggests that L-PBF-SS316L pits have higher stability than wrought SS316L pits. E_{rp} is the potential above which an existing pit can continue grow and ($E_{pit} - E_{rp}$) represents the range of potentials at which stable pit propagation can occur. The current study investigates the underlying microstructural causes for the greater stability of growing pits in L-PBF-SS316L. In the remainder of this section, the pertinent literature is reviewed to provide further context and highlight the rationale behind our work.

It is generally accepted that pitting corrosion occurs in following stages: (i) passive film breakdown, (ii) metastable pitting, (iii) stable pit propagation and possibly (iv) pit stifling/repassivation [9]. The overall pitting resistance of a material in a given environment can be determined either by the breakdown of the passive film to form a metastable pit or the transition of a metastable pit to a stable pit [10]. Potentiodynamic polarization curves for L-PBF-SS316L in neutral chloride environment exhibit numerous metastable pitting events at potentials well below E_{pit}, which is high compared to wrought SS316L [1,7]. This indicates that passive film breakdown events are frequent, but metastable pits do not transition to stable pits until a high anodic potential is applied. Therefore, pit growth stability is expected to play a significant role in determining the overall pitting resistance of L-PBF-SS316L stainless steel.

* Corresponding authors.
E-mail addresses: hariharan.50@osu.edu (K. Hariharan), es3cv@virginia.edu (E.J. Schindelholz).

https://doi.org/10.1016/j.corsci.2023.111668
Received 17 July 2023; Received in revised form 23 October 2023; Accepted 11 November 2023
Available online 15 November 2023
0010-938X/© 2023 Elsevier Ltd. All rights reserved.

Among the features controlling different stages of pitting in L-PBF stainless steels, process-induced defects, such as lack of fusion porosity intersecting the tested surface, largely control stable pit initiation and hence E_{pit}. Schaller and co-workers studied pitting corrosion of L-PBF-SS304L in 0.6 M NaCl using a micro-capillary cell and found that the measured E_{pit} was considerably lower in regions of the build with evident porosity than in pore-free regions [11]. Sun et al. reported that E_{pit} for a high porosity (2–6 vol%) L-PBF-SS316L was lower (~100 mV) in 0.9% NaCl solution than wrought SS316L. In addition to porosity, melt pool boundaries (MPBs), which form between two molten pools during the L-PBF process and are delineated by differences in grain or sub-grain orientation, size and morphology [12], were reported to be sites for pit initiation [5]. However, stable pit initiation took place only at high anodic potentials ($> 0.6\ V_{SCE}$). So, while MPBs may be pit initiation sites, they are activated only at high potentials and might not be sites for pit initiation at potentials close to free corrosion conditions.

While processing defects such as porosity influence pit initiation considerably, heterogeneities such as MPBs, grain boundaries, and dislocation substructure can significantly influence pit growth and repassivation [13]. Among the microstructural heterogeneities, L-PBF stainless steel MPBs have been shown to be the most susceptible to localized attack in various environments. For example, Macantangay et al. showed that the MPBs of L-PBF-SS316L are selectively attacked in ammonium persulfate solution [14]. They speculated that MPBs may be sites of preferential sigma phase and CrN precipitation but did not provide microstructural evidence. Ni et al. also showed selective attack of L-PBF-SS316L MPBs after a 12 h immersion in 6% $FeCl_3$ + 0.05 M HCl [15]. Similarly, Preito et al. observed that MPBs in L-PBF-SS316L underwent severe localized corrosion leading to melt pool fallout during immersion in 6% $FeCl_3$ at 55 °C while not offering any insights into underlying causes [16]. Wang et al. observed pit initiation near MPBs in L-PBF-SS316L and attributed it to inhomogeneous lattice defects associated with high misorientation at MPBs [5]. However, the evidence does not unambiguously establish the reason for corrosion susceptibility because high misorientation regions were also found away from MPBs and they did not serve as pit initiation sites.

While the existing literature reveals that MPBs are susceptible sites in L-PBF-SS316L, the environments studied are not representative of the local pit chemistry, so they provide no insight into the role of MPBs on pit stability and repassivation. Furthermore, previous studies were performed on boldly exposed test coupons, which limits the ability to determine the pit propagation pathways. In this work, we utilize one-dimensional (1D) pit electrodes. 1D pit electrodes are small cross-section samples, usually wires, embedded in epoxy [17–21]. They are also referred to in the literature as artificial pit electrodes or lead-in-pencil electrodes. The entire exposed cross section is activated and, as they dissolve down into the epoxy, the natural pit environment is generated. The transport within the channel created in the epoxy is one-dimensional [17,18]. This electrode geometry also allows for cross-sectioning of the pit bottom to probe the pit propagation pathways.

We demonstrate here that severe selective attack can occur at L-PBF-SS316L MPBs near the critical local pit chemistry for repassivation of L-PBF-SS316L in chloride environments. The selective attack of the MPBs is termed here as inter-melt pool corrosion (IMPC). Analogous to the intergranular corrosion of stainless steel, we attribute this IMPC to depletion of Cr and Mo at MPBs resulting from the L-PBF solidification conditions. We present the results of a series of electrochemical repassivation experiments using 1D pits constructed of L-PBF and wrought SS316L in 0.6 M NaCl to replicate the local pit chemistry and understand the mechanism of corrosion near critical chemistry corresponding to pit repassivation. Close examination of the microstructural attack in these experiments was used to correlate the localized corrosion to the electrochemical behavior. The implications of IMPC on the use and determination of repassivation protection potentials are discussed.

2. Materials and methods

2.1. Materials and additive manufacturing

SS316L powder procured from 3D Systems was processed using an L-PBF technique on a 3D Systems ProX DMP 200 printer to make rectangular parallelepiped prism parts built on a SS316L plate. Each parallelepiped prism part had an edge length of 1.5 cm and the parts were built at an angle of 45° to the build plate normal. A square raster scan strategy was used, with raster pattern rotated by 90° between each layer, repeating every 5th layer. The processing parameters given in Table 1 were used to produce low-porosity parts with > 99% density. The composition of the as-printed L-PBF-SS316L was analyzed by NSL Analytical using inductively coupled plasma - optical emission spectroscopy (ICP-OES) and a LECO Corp. combustion tool. Table 2 lists the composition of the L-PBF-SS316L part, powder used, and the vendor-specified composition of wrought SS316L used in this study.

2.2. 1D pit electrode experiments

Cuboidal 1D pit electrodes with a square surface cross section of 250 μm × 250 μm were constructed from L-PBF and wrought SS316L stainless steels using electrical discharge machining. The orientation of the extracted 1D pit electrode with respect to the parallelepiped build along with an etched optical micrograph showing the melt pool boundaries are shown in Supplementary Figure 1. Each of the L-PBF-SS316L 1D pit electrodes was extracted from the as-built part. A representative SEM image of the unmounted artificial 1D pit electrode is shown in Supplementary Figure 2. The cut surfaces of 1D pit electrodes were ground with 240 grit SiC paper to eliminate residual of the machining wire before mounting in epoxy. The mounting was done in such a way that the square cross-section formed the exposed surface. The surface was ground to 600 grit SiC polishing paper, rinsed, and dried before each experiment.

The polarization experiments were carried out in the vertical configuration following Li et al. [18]. The epoxy cylinders were mounted at the bottom of the cylindrical cell such that the top surface of the cylinder was facing upward in contact with the air-exposed quiescent 0.6 M NaCl electrolyte. A saturated calomel reference electrode (SCE) and Pt mesh counter electrode were inserted from the top of the cell. All experiments were conducted using a Gamry Reference 600+ potentiostat (Gamry Instruments, Warminster, PA) at room temperature (23 ± 2° C).

The following sequence was used for the potentiostatic repassivation experiments on 1D pit electrodes: dissolution was initiated by applying a high potential pulse of + 1.2 V_{SCE} for 5 min, which breaks the passive oxide film in stainless steels. Initiation of the 1D pit dissolution was affirmed from the rapid increase in dissolution current density to greater than 1 $mA.cm^{-2}$. After initiation, the potential was stepped down to+ 0.4 V_{SCE} and held for 3 h to deepen the 1D pit. The initiation and growth potentials were chosen based on previous SS316L stainless steel 1D pit experiments [17,18]. The potential of 0.4 V_{SCE} is well above the nominal E_{rp} of stainless steels in chloride environments (−0.2 V_{SCE} to 0 V_{SCE}) [22]. The pit depth can be calculated based on the charge passed assuming 100% faradaic efficiency and uniform, congruent dissolution

Table 1
L-PBF process parameters utilized in this study.

Laser power	110 W
Laser velocity	1400 mm/s
Layer thickness	30 μm
Laser focus offset	+ 1 mm
Mean beam diameter at focus	12 μm

Table 2
Composition of the as-built L-PBF-SS316L, feedstock powder and the wrought SS316L used in this study.

	Fe	Cr	Ni	Mo	Mn	Si	N	O	P	C	S	Al
L-PBF	67.5	17.3	11.1	2.16	1.07	0.65	0.093	0.063	0.019	0.017	0.009	0.003
SD	0.34	0.35	0.22	0.20	0.12	0.098	0.014	0.0094	0.0029	0.003	0.001	0.0005
Powder	68.4	16.9	10.6	2.10	1.09	0.66	0.110	0.093	0.018	0.021	0.011	0.012
SD	0.34	0.85	0.53	0.10	0.05	0.033	0.017	0.014	0.003	0.003	0.002	0.002
Wrought	68.8	16.8	10.1	2.11	1.46	0.60	0.039	0.0049	0.028	0.022	0.001	0.021

across the exposed area.

Following the initial growth, the applied potential was stepped down to + 0.1 V_{SCE} and then down to −0.35 V_{SCE} in steps of 0.01 V following potentiostatic hold at each potential for 1 h. This sequence is loosely based on the ASTM-G192 or Tsujikawa-Hisamatsu Electrochemical (THE) method [23]. The tests were repeated five times for reproducibility.

The following sequence was used for the potentiostatic experiments conducted below the nominal repassivation potential. The pit was initiated by applying a voltage pulse of + 1.2 V_{SCE} for 5 min and the initial pit growth was carried out at + 0.4 V_{SCE} for 5 h. Following the initial growth, the applied potential was stepped down to −0.1 V_{SCE} which was approximately 0.03 V below the measured E_{rp} for L-PBF-SS316L based on 5 replicated experiments.

Potentiodynamic polarization experiments were performed to distinguish complete and incomplete repassivation using the steps for pit initiation and growth as described previously, except that the pit was grown at + 0.45 V_{SCE} for 4 h. A downward potentiodynamic scan was conducted at a scan rate of 0.1 mV/s from + 0.45 V_{SCE} to a −0.18 V_{SCE}, which was about 0.09 V below the nominal E_{rp} of both L-PBF and wrought SS316L but still above the zero current potential (ZCP) of the pit. The potential choice allowed for either complete repassivation or deactivation to occur. The downward potentiodynamic polarization was followed by potentiostatic hold at −0.18 V_{SCE} for 2 h to ensure the pits had enough time to fully dilute below the critical chemistry for pit stability, C_{crit} [6]. The potentiostatic polarization was followed by an upward polarization scan at a rate of 1 mV/s. The experiments were designed based on previous work by Jun et al. [24].

2.3. Microstructural characterization

2.3.1. Scanning electron microscopy

The epoxy cylinder was abraded parallel to its axis on 120 grit SiC paper to approach the corroded 1D pit bottom. Once the wall of the 1D pit was reached, the cross-section was ground successively to 1200 grit using SiC paper followed by fine polishing with 6 μm, 3 μm, and 1 μm diamond paste dispersed in extender. The final polishing was carried out in 0.05 μm colloidal silica suspension on a vibratory polisher. The corroded cross-section was imaged under a Thermo Fisher Scientific Apreo FEG scanning electron microscope (SEM) at a working distance of 10 mm at an accelerating voltage of 10 kV using the low-vacuum secondary electron detector. The chamber was filled with water vapor such that the chamber pressure of 50 Pa was maintained. Low-vacuum mode was used to avoid charging of the non-conductive epoxy surface which remained beneath the corroded part of the 1D pit.

To establish a baseline for the analysis of the corrosion morphology, an uncorroded etched cross-section of the 1D pit electrode was additionally imaged under the SEM. The preparation involved the same steps as above and additionally the sample was electrolytically etched in 10% oxalic acid at + 5 V for 2 min. The epoxy cylinder surrounding the sample was coated with carbon to make it conductive and imaging was conducted at 10 kV in the back-scattered electron mode at a working distance of 10 mm. In addition to the characterization of the 1D pit electrodes, etched parallelepiped coupons were also imaged following the procedure described above.

2.3.2. Characterization of the melt pool boundary – scanning transmission electron microscopy (STEM)

The L-PBF-SS316L was ground to 1200 grit SiC paper before electrolytically etching the surface parallel to the build direction in a freshly prepared solution that contained 85% orthophosphoric acid, 96% concentrated sulfuric acid, and DI water in a volume ratio of 5:2:3 in a two-electrode cell with the L-PBF-SS316L as the working electrode with graphite rod as counter electrode [25]. A constant current density of 500 $mA \bullet cm^{-2}$ was applied to the sample for 120 s to reveal the location of the MPBs in the sample. Cross-sectional samples for the transmission electron microscopy were extracted using a conventional focused ion beam (FIB) lift-out method in a Helios NanoLab 600 DualBeam. Further thinning was carried out at 900 and 500 eV utilizing the Fischione 1040 Nanomill to minimize the surface amorphous layer and subsurface damage. The cross-section was taken from a location in the sample such that the MPB was included in the cross-section with melt pools on either side of the boundary. STEM images and spectroscopy were collected using a 6 probe-aberration corrected Thermo Fisher Scientific Themis Z S/TEM operated at 300 kV, 18.9 mrad convergence semi-angle. The EDX maps for Fe, Ni, Cr, and Mo were collected for 2 h to ensure sufficient counts.

3. Results and discussion

The as-built L-PBF-SS316L used in this study exhibited features typical of material produced by the powder bed process. The feedstock and process parameters described in Tables 1 and 2 produced materials with > 99% density. The MPBs are seen in the polished and etched surface in Fig. 1a. A FIB lift-out was cut from a region of this sample surface that contained an etched MPB, as indicated in Fig. 1b. The arrow in the high-angle annular dark field-scanning transmission electron microcopy (HAADF-STEM) image of the liftout in Fig. 1c is located in the etch trench (divot) and points to the location of the MPB. Homogenously distributed inclusions are also visible in this image as dark dots. These inclusions were identified as oxides in a previous microstructural study of the same material [25]. The EDS imaging and line scan in Fig. 1d-f show depletion of Cr and, possibly, Mo at the MPB. This finding is consistent with previous reports of Cr and Mo MPB depletion in L-PBF-SS316L [26,27].

1D pit electrodes were constructed from the as-built L-PBF and wrought SS316L to assess the relative electrochemical repassivation behavior of these materials. The strict geometry of the 1D pit electrodes allows creation of electrochemical conditions that enable well-controlled pit growth and local chemistry [18,21,28]. For this study, corrosion was initiated in the 1D electrodes and their repassivation behavior examined using stepped potential experiments, as described above.

The modified-THE tests using the 1D pit electrodes indicate that both the L-PBF-SS316L and the wrought SS316L had nominally similar repassivation potentials. The repassivation potential, E_{rp}, is defined as the potential at which the current drops during the hold and does not rise in subsequent steps. The current drop is an indication that the metal dissolution at pit bottom is unable to sustain the critical local pit chemistry. The current definition of E_{rp} is based on the understanding that repassivation kicks in when the dissolution at the pit bottom is unable to outrun the dilution of the pit by outward diffusion of metal

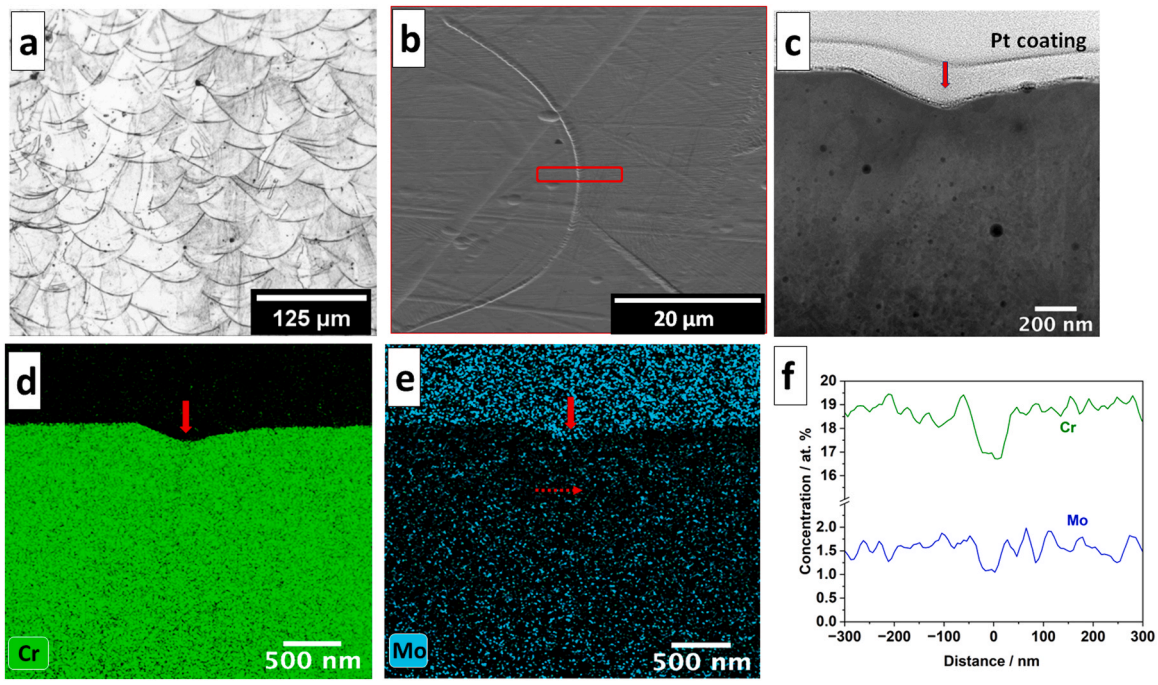

Fig. 1. (a) Etched SEM micrograph of L-PBF-SS316L showing melt pool boundaries(MPBs), (b) high-magnification SEM micrograph showing the location of the FIB lift-out cutting across an etched MPB, (c) HAADF-STEM micrograph showing nano-scale oxide inclusions with the location of MPB indicated by a red arrow, (d) EDX map of Cr showing depletion at the MPB, (e) EDX map of Mo showing faint contrast of its depletion at the MPB, (f) 1D EDX line scan showing the variation of Cr and Mo along the dashed arrow shown in (e).

cations.

The results of representative experiments in Fig. 2 show that these conditions were met at −0.07 V_{SCE} for L-PBF (a) and −0.1 V_{SCE} for the wrought material (b). The average E_{rp} determined over 5 replicate tests for L-PBF and wrought SS316L were −0.074 ± 0.005 V_{SCE} and −0.094 ± 0.005 V_{SCE}, respectively.

Holding the 1D L-PBF-SS316L pits at ~0.03 V below the average E_{rp} measured via the modified THE tests (−0.1 V_{SCE}) for longer times, however, resulted in increasing current for up to 8 h, Fig. 3. This contrasts with wrought SS316L pits where the current density diminished to less than 10^{-4} A.cm^{-2} within an hour while holding ~ 0.03 V below their average E_{rp} (−0.12 V_{SCE}). These long-term potential hold tests were preceded by anodic polarization at + 0.4 V_{SCE} to grow the pits to a depth of ~1200 µm to ensure consistency with the modified THE tests. The trends in Fig. 3 were reproducible across three replicate experiments for each material.

The rising current of the L-PBF-SS316L pits during the long-term potential holds is indicative of incomplete repassivation associated with activation-controlled pit growth. The works of Starr et al. [29] and Jun et al. [24] provide critical insights into the expected behavior of a fully repassivated pit versus a pit that has not fully repassivated. Based on these studies, it can be inferred that, during potentiostatic polarization of a completely repassivated pit near the repassivation potential, the current should decrease and remain in the passive state, as seen for the wrought SS316L in Fig. 3. On the other hand, current would continue to increase with time as a result of active dissolution for a pit that has not attained a state of complete repassivation, as seen for the L-PBF-SS316L in Fig. 3. A fundamental explanation for this is that, as the pit deepens under potentiostatic conditions, the surface metal cation concentration, C_{surf}, will increase. The zero current potential (ZCP) of

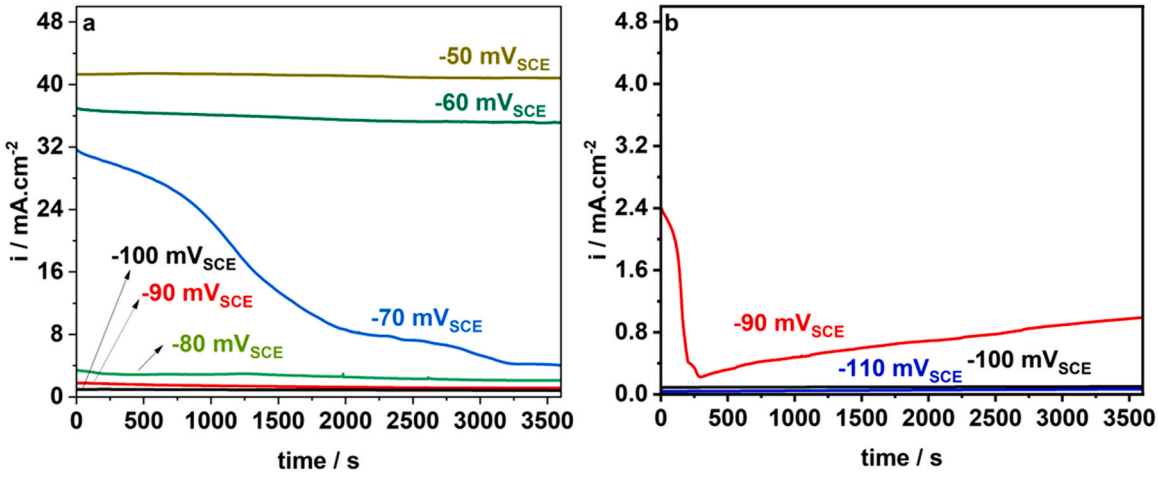

Fig. 2. Repassivation behavior of (a) L-PBF-SS316L and (b) Wrought SS316L 1D pits grown to ≈1200 µm in 0.6 M NaCl at 23 °C when tested according to modified-ASTM-G192 test [7].

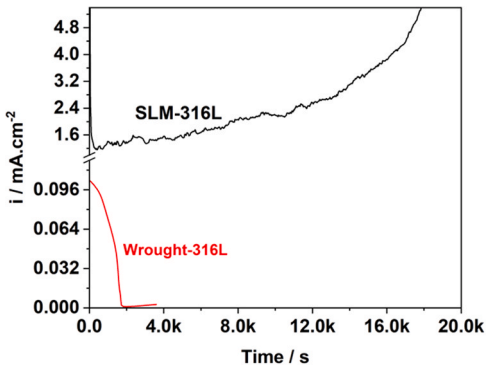

Fig. 3. Potentiostatic polarization of L-PBF-SS316L and wrought SS316L 1D pits in 0.6 M NaCl at 23 °C at a potential 0.03 V below the nominal E_{rp}. The pits were pre-grown to ≈1200 μm prior to this experiment.

the pit decreases with increase in the surface metal cation concentration, which increases the overpotential for anodic dissolution over time when the applied potential, E_{app}, is held constant. This causes the rate of anodic dissolution at the pit bottom to increase with time [18]. It is noteworthy that activation-control pit growth is a transient state, and a pit would tend to transition to diffusion-limited pit growth at longer times [18,20,30].

Cross-sectioning of an L-PBF-SS316L 1D pit bottom after one of the 8 h potentiostatic hold tests revealed selective attack of the melt pool boundaries, Fig. 4. The fish-scale morphology of the MPBs is evident from the trace of the corrosion front, Fig. 4b. The size and orientation of the MPBs are consistent with the etched uncorroded L-PBF-SS316L 1D pit electrode seen in Fig. 4a. It is noteworthy that the pit morphology is tapered. The tapering may be caused by deviation from 1D diffusion at the pit bottom due to selective MPB attack. This could have led to melt pool fall-out near the pit bottom or crevice corrosion at the metal/epoxy interface. It must be pointed out that none of the L-PBF 1D pit cross-sections examined in this work had evident lack-of-fusion pores in them. Moreover, it is unlikely that any of L-PBF pits had intersected a void during the polarization experiments because such an intersection would leave an electrochemical signature.

Fig. 5 shows a cross-section of a wrought pit bottom exhibiting crystallographic attack after the potentiostatic hold test shown in Fig. 3. Crystallographic attack is consistent with the morphology of a repassivated pit that was under charge-transfer control before repassivation [18,31,32]. Repassivation of the wrought pit likely proceeded in two steps when the potential was dropped from $+0.4\ V_{SCE}$ down to $-0.12\ V_{SCE}$ during the experiments: (i) the pit surface lost its salt film and dissolution was transiently under charge-transfer control, leading to crystallographic morphology, (ii) final repassivation when the pit then diluted below the critical chemistry for repassivation [18,28]. The cross-section of wrought SS316L also shows tapering similar to that seen in L-PBF-SS316L, Fig. 4, which might be due crevice corrosion at the metal/epoxy interface or non-uniform crystallographic attack during charge-transfer controlled pit growth. The potentiostatic polarization behavior of the L-PBF-SS316L and wrought SS316L seen in Fig. 3 are vastly different but both exhibited crevice corrosion at the metal/epoxy interface leading to the tapering of pit bottom. Therefore, it is

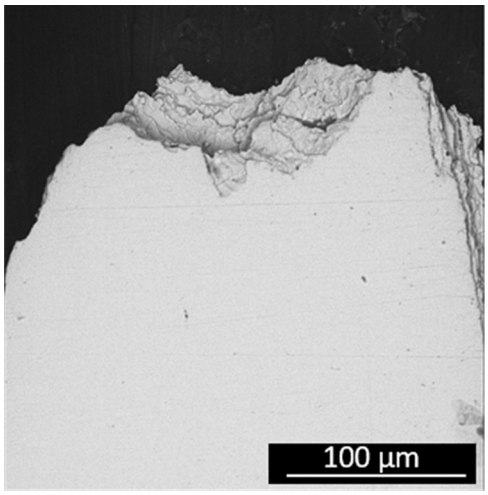

Fig. 5. Post-corrosion cross-section of a wrought SS316L 1D pit after potentiostatic polarization at $-0.12\ V_{SCE}$ showing crystallographic morphology.

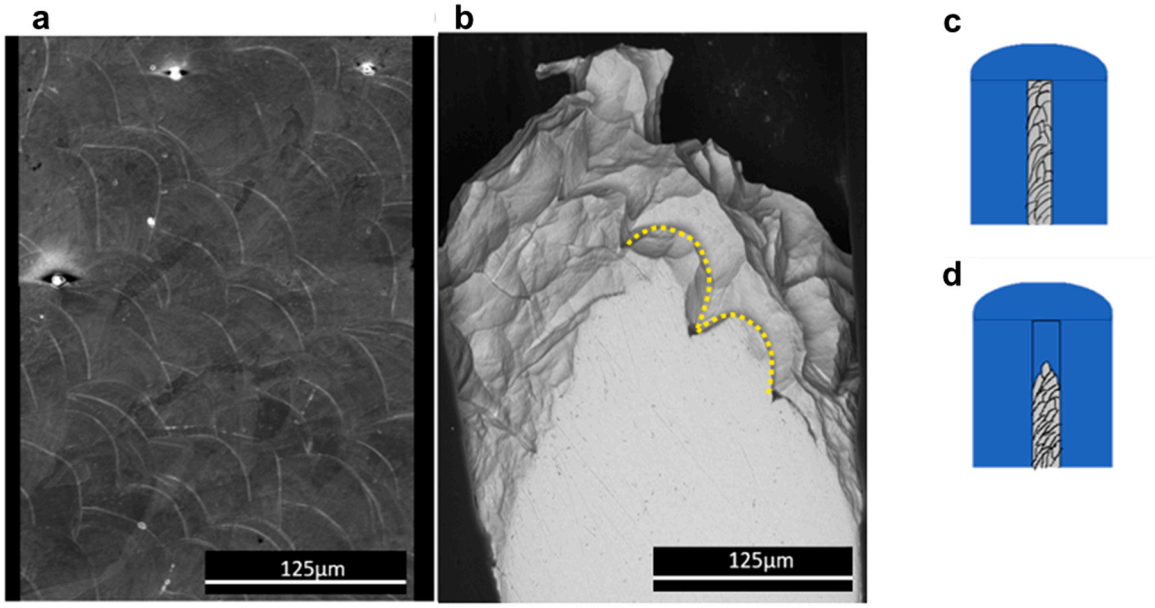

Fig. 4. Cross-section of the L-PBF-SS316L 1D pit with its surface etched showing the meltpool boundary b) Post-corrosion cross-section of L-PBF-SS316L 1D pit after 8 h hold at $-0.1\ V_{SCE}$ after the pit was grown to 1200 μm showing selective propagation of attack along the meltpool boundaries (yellow outline). Schematics (c) and (d) correspond to (a) and (b) respectively.

reasonable to assume that the crevice corrosion was not the cause for high currents observed in Fig. 3 for L-PBF-SS316L. The tapering of 1D pit bottom cross-section was also observed in our previous work on 17–4 PH stainless steel, but it is probably more of an issue for larger cross section electrodes than for 1D pits made from fine wires [33].

Potentiodynamic polarization experiments designed to examine the reactivation behavior of the 1D pits provide further evidence of incomplete repassivation of the L-PBF-SS316L down to at least −0.18 V_{SCE}, 0.09 V below the E_{rp} determined by the potential step experiments. Fig. 6 shows the results of these experiments wherein the upward scan of an L-PBF-SS316L 1D pit after a 2 h hold at −0.18 V_{SCE} exhibits immediate reactivation while the wrought specimen remains passive. These experiments were based on work by Jun et al., who showed a clear distinction between partial and complete repassivation could be made through upward potentiodynamic polarization of pits after the pit current density had dropped to low values ($< 10^{-4}$ A.cm^{-2}) [24].

The behavior seen in Fig. 6 indicates that the L-PBF-SS316L pit did not completely repassivate even when the pit chemistry was diluted, while the wrought material underwent full repassivation. The results presented so far in this study provide important additional insight that the attainment of apparent C_{crit} of the alloy does not guarantee complete repassivation of all the local microstructural features. This suggests that Cr-depleted MPBs were actively corroding even when the pit had diluted, leading to partial repassivation.

It is pertinent to discuss the work of Starr et al. on binary Fe-Cr alloys that correlated the existence of partial repassivation behavior to bulk alloy composition [29]. They found that alloys with 12 wt% Cr did not completely repassivate when the chloride concentration exceeded 1 M, but remained in a deactivated state, whereby the pit bottom was essentially at the ZCP of the bare metal surface free from a protective oxide film. On the other hand, pits in alloys containing 16.9 wt% Cr underwent full repassivation irrespective of chloride concentration in the range of 10^{-2} - 1 M. In their study, the deactivated alloy spontaneously reactivated with small perturbation of potential in the anodic direction. The behavior of low-Cr binary Fe-Cr in concentrated chloride environment is similar to the behavior of L-PBF-SS316L seen in Fig. 6, which showed immediate reactivation, whereas the wrought SS316L behaves similar to the high-Cr alloy in the work of Starr et al.

The results of this study, taken together, lead us to attribute the incomplete repassivation behavior of L-PBF-SS316L to selective attack of the MPBs, or IMPC. The origin of this selective attack appears to be the Cr (and possibly Mo) depletion at the MPBs, Fig. 1. Depletion of these passivating elements at MPBs is a common feature of L-PBF-SS316L and results from the rapid solidification conditions [26,27]. Although others have speculated that selective MPB attack could be due to additional factors, such as local residual stress gradients or secondary phase precipitates, evidence of such has not been found to date [14–16]. This IMPC phenomenon appears mechanistically similar to intergranular corrosion in sensitized austenitic stainless steel and Ni-Cr-Mo alloys, wherein Cr (and possibly Mo) depletion at the grain boundaries leads to their selective attack.

The evidence presented in this study can explain the enhanced pit growth stability of L-PBF-SS316L observed in previous studies. MPBs serve as susceptible sites for continued dissolution that remain active even when rest of the alloy is repassivated. Continued propagation along MPBs might be the underlying cause behind the large hysteresis and lower E_{rp} reported in cyclic potentiodynamic polarization curves [1,2,7]. This is also the likely reason behind literature reports that E_{rp} of L-PBF-SS316L was below its forward scan ZCP [1,7]. This implies that selective pit propagation along MPBs or IMPC makes the L-PBF-SS316L susceptible to pitting corrosion close to practically relevant free corrosion conditions.

The experimental results also highlight that the local repassivation potentials of different microstructural features play an important role in deciding the susceptibility of the alloy to localized corrosion in a given environment, which contrasts what has been suggested in the literature [34,35]. Anderko and Sridhar developed a model that calculated the local repassivation potential based on the local Cr (and Mo) concentration as a function of the distance from the grain boundary in a sensitized stainless steel and spatially integrated the local repassivation potentials to calculate the nominal repassivation potential of the alloy. In their study, the width of the Cr-depletion region in a Ni-base alloy (alloy 600) was of the order of a few nm, whereas the pit size at repassivation was of the order of tens to hundreds of μm. Thus, averaging of the repassivation potential of the Cr-depleted region with the bulk Cr-containing matrix resulted in a lack of sensitivity of the repassivation potential with heat treatment for that alloy. However, for a 22% Cr duplex stainless steel, the width of the Cr, Mo, and N depleted region due to sigma phase formation was much larger and assumed values closer to the pit size [35]. In that case, they found that the nominal repassivation potential of the alloy decreased significantly with secondary phase formation.

In this work, however, we report that a nano-scale (85 nm) depletion of passivating elements at the melt pool boundary in L-PBF-SS316L as seen in Fig. 1 f makes it more susceptible to localized corrosion well below the E_{rp} than wrought SS316L despite their nominal repassivation potentials being similar. This suggests that repassivation potential of the most susceptible microstructural feature dictates the localized corrosion performance of the alloys. The use of the nominal E_{rp} measured by

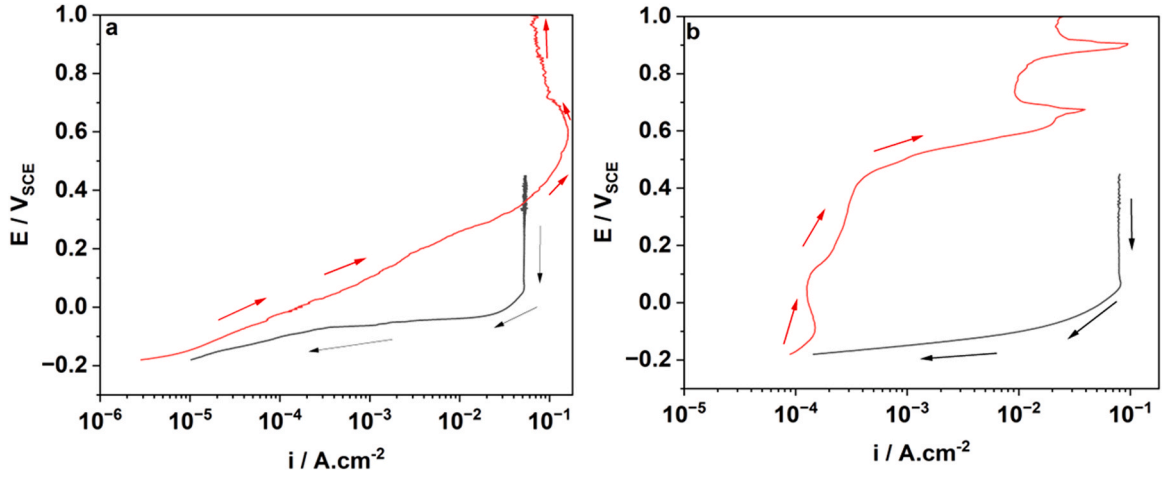

Fig. 6. Potentiodynamic polarization of (a) L-PBF-SS316L and (b) Wrought SS316L 1D pits in 0.6 M NaCl at 23 °C. The pits were pre-grown to ≈1200 μm prior to this experimental sequence. The pits were potentiostatically held at −0.18 V_{SCE} for 2 h in between the downward (black) and upward (red) potentiodynamic scans.

polarization methods designed for wrought alloys as a qualification metric for L-PBF stainless steels might result in situations that severely compromise the structural integrity of the alloy. An alternative qualification metric could involve long-term tests in simulated service environments.

One possible solution to mitigate the risk of IMPC is to eliminate the melt pool boundaries by heat treatment of the as-built material. For instance, Zhou et al. reported that medium-temperature annealing at 950^0 C for 4 h followed by furnace cooling eliminated the MPBs in L-PBF-SS316L while it did not alter the grain size and morphology [3]. On subsequent testing, they found that this heat treatment enhanced both mechanical properties and pitting potentials, which was attributed to elimination of MPBs without loss of solidification grain structure. However, one must be careful that deleterious phases including oxides are not precipitated by such treatment. Recently, Guo et al. showed that nano-scale oxides precipitated following 1 h annealing at 900 °C, which might have possible implications for mechanical as well as corrosion properties [25]. Designing heat treatments for the balance of corrosion and mechanical properties in L-PBF-SS316L remains an area worthy of continued investigation.

4. Conclusions

The study examined the role of melt pool boundaries in L-PBF-SS316L stainless steel repassivation behavior in chloride media. The combined microstructural characterization results and electrochemical 1D pit experiments lead to the following conclusions:

- Based on the electrochemical and morphological evidence, L-PBF-SS316L undergoes inter-melt pool corrosion below the nominal repassivation potential in local pit chloride environment. This is due to the phenomenon of partial repassivation of L-PBF-SS316L 1D pits where the melt pool boundaries continue to undergo active corrosion while rest of the alloy had undergone repassivation.
- IMPC is attributed to Cr-,Mo-depletion at the melt pool boundaries, a consequence of L-PBF-SS316L processing resulting from solute partitioning during solidification.
- The selective pit propagation along MPBs could make L-PBF-S316L more susceptible to pitting corrosion under practically relevant free corrosion conditions, undermining the material's localized corrosion performance.
- The results of this study suggest that the selective attack of melt pool boundaries due to partial repassivation of L-PBF-SS316L melt pool might significantly deteriorate the structural integrity and performance of L-PBF-SS316L components. The results could also be extended to microstructural heterogeneities in other alloys.

CRediT authorship contribution statement

Karthikeyan Hariharan: Conceptualization, Methodology, Investigation, Writing – original draft, Visualization. **Xiaolei Guo**: Methodology, Investigation, Writing – review & editing. **Hsien-Lien Huang:** Investigation, Visualization, Writing – review & editing. **Narasi Sridhar:** Methodology, Conceptualization, Writing – review & editing. **Jayendran Srinivasan:** Methodology, Investigation, Writing – review & editing. **Jinwoo Hwang:** Methodology, Supervision, Fund acquisition, Writing – review & editing. **Gerald S. Frankel:** Conceptualization, Supervision, Writing – review & editing. **Eric J. Schindelholz:** Conceptualization, Supervision, Project administration, Funding acquisition, Writing – review & editing.

Declaration of Competing Interest

The authors declare that they have no known competing financial interests or personal relationships that could have appeared to influence the work reported in this paper.

Data availability

Data will be made available on request.

Acknowledgements

The authors would like to thank Dr. Michael Melia (Sandia National Laboratories) and Dr. Bradley Jared (University of Tennessee) for supplying the L-PBF-SS316L samples. Electron microscopy was performed at the Center for Electron Microscopy and Analysis (CEMAS) at The Ohio State University. H.H and J.H acknowledge partial support from the Center for Emergent Materials, an NSF MRSEC, under award number DMR-2011876.

Appendix A. Supporting information

Supplementary data associated with this article can be found in the online version at doi:10.1016/j.corsci.2023.111668.

References

[1] Q. Chao, V. Cruz, S. Thomas, N. Birbilis, P. Collins, A. Taylor, P.D. Hodgson, D. Fabijanic, On the enhanced corrosion resistance of a selective laser melted austenitic stainless steel, Scr. Mater. 141 (2017) 94–98.
[2] G. Sander, S. Thomas, V. Cruz, M. Jurg, N. Birbilis, X. Gao, M. Brameld, C. Hutchinson, On the corrosion and metastable pitting characteristics of 316L stainless steel produced by selective laser melting, J. Electrochem. Soc. 164 (2017) C250.
[3] C. Zhou, S. Hu, Q. Shi, H. Tao, Y. Song, J. Zheng, P. Xu, L. Zhang, Improvement of corrosion resistance of SS316L manufactured by selective laser melting through subcritical annealing, Corros. Sci. 164 (2020), 108353.
[4] Y. Zhang, J. Zhang, Q. Yan, L. Zhang, M. Wang, B. Song, Y. Shi, Amorphous alloy strengthened stainless steel manufactured by selective laser melting: enhanced strength and improved corrosion resistance, Scr. Mater. 148 (2018) 20–23.
[5] K. Wang, Q. Chao, M. Annasamy, P.D. Hodgson, S. Thomas, N. Birbilis, D. Fabijanic, On the pitting behaviour of laser powder bed fusion prepared 316L stainless steel upon post-processing heat treatments, Corros. Sci. 197 (2022), 110060.
[6] F. Andreatta, A. Lanzutti, E. Vaglio, G. Totis, M. Sortino, L. Fedrizzi, Corrosion behaviour of 316L stainless steel manufactured by selective laser melting, Mater. Corros. 70 (2019) 1633–1645.
[7] M. Laleh, A.E. Hughes, W. Xu, I. Gibson, M.Y. Tan, Unexpected erosion-corrosion behaviour of 316L stainless steel produced by selective laser melting, Corros. Sci. 155 (2019) 67–74.
[8] J. Stewart, D.E. Williams, The initiation of pitting corrosion on austenitic stainless steel: on the role and importance of sulphide inclusions, Corros. Sci. 33 (1992) 457–474.
[9] G. Frankel, Pitting corrosion of metals: a review of the critical factors, J. Electrochem. Soc. 145 (1998) 2186.
[10] G.S. Frankel, T. Li, J.R. Scully, Perspective—localized corrosion: passive film breakdown vs pit growth stability, J. Electrochem. Soc. 164 (2017) C180.
[11] R.F. Schaller, A. Mishra, J.M. Rodelas, J.M. Taylor, E.J. Schindelholz, The role of microstructure and surface finish on the corrosion of selective laser melted 304L, J. Electrochem. Soc. 165 (2018) C234.
[12] K. Sommer, L. Agudo Jácome, R. Hesse, D. Bettge, Revealing the nature of melt pool boundaries in additively manufactured stainless steel by nano-sized modulation, Adv. Eng. Mater. 24 (2022) 2101699.
[13] E.J. Schindelholz, M.A. Melia, J.M. Rodelas, Corrosion of additively manufactured stainless steels—process, structure, performance: a review, Corrosion 77 (2021) 484–503.
[14] D.A. Macatangay, S. Thomas, N. Birbilis, R.G. Kelly, Unexpected interface corrosion and sensitization susceptibility in additively manufactured austenitic stainless steel, Corrosion 74 (2017) 153–157.
[15] X.-Q. Ni, D.-C. Kong, Y. Wen, L. Zhang, W.-H. Wu, B.-B. He, L. Lu, D.-X. Zhu, Anisotropy in mechanical properties and corrosion resistance of 316L stainless steel fabricated by selective laser melting, Int. J. Miner. Metall. Mater. 26 (2019) 319–328.
[16] C. Prieto, M. Singer, T. Cyders, D. Young, Investigation of pitting corrosion initiation and propagation of a type 316L stainless steel manufactured by the direct metal laser sintering process, Corrosion 75 (2018) 140–143.
[17] J. Srinivasan, R.G. Kelly, Evaluating the critical chemistry for repassivation at the corroding surface using mass transport model-based artificial Pit experiments, J. Electrochem. Soc. 163 (2016) C768–C777.
[18] T. Li, J.R. Scully, G.S. Frankel, Localized corrosion: passive film breakdown vs Pit growth stability: Part V. Validation of a new framework for Pit growth stability using one-dimensional artificial Pit electrodes, J. Electrochem. Soc. 166 (2019) C3341–C3354.
[19] G. Gaudet, W. Mo, T. Hatton, J. Tester, J. Tilly, H.S. Isaacs, R. Newman, Mass transfer and electrochemical kinetic interactions in localized pitting corrosion, AlChE J. 32 (1986) 949–958.

[20] N.J. Laycock, R.C. Newman, Localised dissolution kinetics, salt films and pitting potentials, Corros. Sci. 39 (1997) 1771–1790.
[21] R.C. Newman, H.S. Isaacs, Diffusion-coupled active dissolution in the localized corrosion of stainless steels, J. Electrochem. Soc. 130 (1983) 1621–1624.
[22] C. Nyby X. Guo J.E. Saal S.-C. Chien A.Y. Gerard H. Ke T. Li P. Lu C. Oberdorfer S. Sahu S. Li C.D. Taylor W. Windl J.R. Scully G.S. Frankel. Electrochemical metrics for corrosion resistant alloys, Scientific Data 8 2021 58.
[23] Standard Test Method for Determining the Crevice Repassivation Potential of Corrosion-Resistant Alloys Using a Potentiodynamic-Galvanostatic-Potentiostatic Technique, in: ASTM standard G-192, ASTM International, West Conshohocken, PA, 2020.
[24] J. Jun, T. Li, G.S. Frankel, N. Sridhar, Corrosion and repassivation of Super 13Cr stainless steel in artificial 1D pit electrodes at elevated temperature, Corros. Sci. 173 (2020), 108754.
[25] X. Guo, H.-L. Huang, M. Zhu, K. Hariharan, S.-C. Chien, N. Huynh, J. Hwang, W. Windl, C.D. Taylor, E.J. Schindelholz, G.S. Frankel, Interstitial elements created via metal 3D printing, Mater. Today 66 (2023) 92–104.
[26] M. Godec, S. Zaefferer, B. Podgornik, M. Šinko, E. Tchernychova, Quantitative multiscale correlative microstructure analysis of additive manufacturing of stainless steel 316L processed by selective laser melting, Mater. Charact. 160 (2020), 110074.
[27] Y. Zhong, L. Liu, S. Wikman, D. Cui, Z. Shen, Intragranular cellular segregation network structure strengthening 316L stainless steel prepared by selective laser melting, J. Nucl. Mater. 470 (2016) 170–178.
[28] J. Srinivasan, R.G. Kelly, On a recent quantitative framework examining the critical factors for localized corrosion and its impact on the galvele Pit stability criterion, Corrosion 73 (2017) 613–633.
[29] K.K. Starr, E.D. Verink Jr., M. Pourbaix, The significance of the protection potential for Fe-Cr alloys at room temperature, Corrosion 32 (1976) 47–51.
[30] G.S. Frankel, L. Stockert, F. Hunkeler, H. Boehni, Metastable pitting of stainless steel, Corrosion 43 (1987) 429–436.
[31] N. Sato, The stability of pitting dissolution of metals in aqueous solution, J. Electrochem. Soc. 129 (1982) 260.
[32] S. Sahu, O.J. Swanson, T. Li, A.Y. Gerard, J.R. Scully, G.S. Frankel, Localized corrosion behavior of non-equiatomic NiFeCrMnCo multi-principal element alloys, Electrochim. Acta 354 (2020), 136749.
[33] K. Hariharan, X. Guo, J. Srinivasan, G.S. Frankel, E.J. Schindelholz, Role of copper on repassivation of stainless steel Pits, J. Electrochem. Soc. 170 (2023), 071503.
[34] A. Anderko, N. Sridhar, G. Tormoen, Localised corrosion of heat-treated alloys Part II – Predicting grain boundary microchemistry and its effect on repassivation potential, Corros. Eng. Sci. Technol. 45 (2010) 204–223.
[35] N. Sridhar, G. Tormoen, S. Hackney, A. Anderko, Effect of aging treatments on the repassivation potential of duplex stainless steel S32205, Corrosion 65 (2009) 650–662.